Non-linear bending compliance of thin ply composite beams by local compression flange buckling

Schadt, F.; Rueppel, M.; Brauner, C.; Courvoisier, Y.; Masania, K.; Dransfeld, C.

DOI
10.1016/j.compstruct.2020.111995

Publication date
2020

Document Version
Final published version

Published in
Composite Structures

Composite Structures 239 (2020) 111995

Contents lists available at ScienceDirect

Composite Structures

journal homepage: www.elsevier.com/locate/compstruct

Non-linear bending compliance of thin ply composite beams by local compression flange buckling

F. Schadt[a], M. Rueppel[a,1], C. Brauner[a], Y. Courvoisier[b], K. Masania[a,*], C. Dransfeld[a,*]

[a] Institute of Polymer Engineering, FHNW University of Applied Sciences and Arts Northwestern Switzerland, Klosterzelgstrasse 2, CH-5210 Windisch, Switzerland
[b] ENATA Industries FZE, Inner Harbour Plot HD-15, Hamriyah Free Zone, Sharjah, United Arab Emirates

ARTICLE INFO

Keywords:
Shape-adaptation
Non-linear compliance
Buckling
Post-buckling
Thin ply composites

ABSTRACT

Passive spanwise bending shape-adaption has the potential to increase the efficiency and manoeuvrability of vehicles with wing-like structures. By utilisation of compression flange buckling, the in-plane stiffness can be tuned to design beams with contrasting pre-buckling and post-buckling bending stiffness. The investigated concept is experimentally validated using a thin-ply laminated composite four-point bending beam, which is designed to experience compression flange buckling in the span with constant moment. The bending stiffness was reduced by more than 41% after the onset of buckling which shows the effectiveness of compression flange buckling for non-linear bending compliance.

1. Introduction

Compliant mechanisms are of increasing importance for lightweight, shape-adaptable applications due to their advantages over conventional pin-jointed mechanisms. The main advantages are increased wear resistance, fewer assembly steps and improved strength-to-weight ratios [1]. Such mechanisms have the potential to improve performance and efficiency over conventional designs through continuous geometry optimization during operation [2].

New materials such as alloys and polymers with shape memory have increased the performance of compliant mechanisms and driven their use in shape-adaptable structures, while advancements in high-performance materials are enabling the better utilisation of intrinsic strength [3–5] and shaping freedom [6,7]. However, a major drawback of compliant mechanisms are their low load-carrying capability. It is challenging to increase the load bearing capability whilst maintaining a large deformability that is needed for compliant mechanisms.

The deformation of compliant mechanisms has so far been actively controlled using conventional actuators or structurally integrated using e.g. smart materials [8]. In applications such as wind turbine blades [9] or marine propellers [10], passively shape-adaptable wing-like structures have been controlled by the structural response to externally applied loads. A common mode of passive shape-adaptation is achieved by changing the angle of attack in accordance to an externally applied load. One design method for this mode is the use of bend-twist coupling effects in unbalanced composite lay-ups which can be readily integrated in fibre-reinforced composite structures [9]. A second design method for passive shape-adaptation is to allow for local elastic instabilities due to buckling or snap-through in the structure [11,12]. Such local elastic instabilities may cause a change in stiffness of the structure and therefore change the deformation mode. Instabilities caused by buckling are often regarded as a failure mode but with composite materials the post-buckling regime can be reached repeatably without the initiation of damage [13], making it an attractive design method for shape-adapting structures.

A less researched mode of shape-adaptation is span-wise bending which is mainly of interest for variable-cant winglets for aircraft [2]. Span-wise bending wing-like structures capable of large continuous deformations are reported for designs which enable large bending deformations by dividing a rigid wing into segments. These wing segments are linked by hinges allowing single [14–17] or multiple degrees of freedom [18]. Actuating the swing can then be realized either using mechanical levers [14] and servomotors [15] or shape memory alloys which expand or contract due to a temperature change caused by electrical resistive heating [16,17]. Despite these valuable examples, applications for span-wise bending shape-adaptation have yet to be reported for highly-loaded structures such as full-scale aircraft wings, wind turbine blades [19] or hydrofoils. In performance sailing

* Corresponding authors present address at: Aerospace Manufacturing Technologies, Faculty of Aerospace Engineering, Delft University of Technology, Kluyverweg 1, 2629 HS Delft, The Netherlands.
E-mail addresses: k.masania@tudelft.nl (K. Masania), C.A.Dransfeld@tudelft.nl (C. Dransfeld).
[1] Present address: Gramazio Kohler Research Professorship for Architecture and Digital Fabrication, ETH Zürich HIB E 43 Stefano-Franscini-Platz 1, CH-8093 Zürich, Switzerland.

https://doi.org/10.1016/j.compstruct.2020.111995
Received 14 December 2019; Accepted 27 January 2020
Available online 07 February 2020

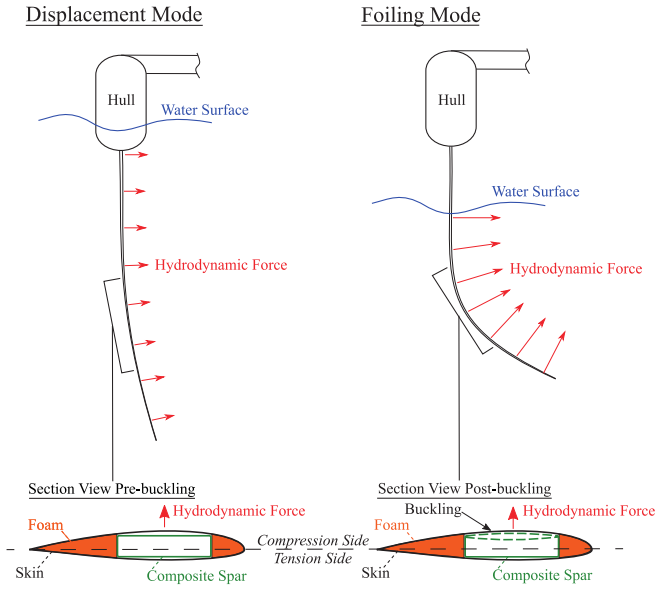

Fig. 1. Structural response of the hydrofoil at low and high speeds. The non-linear compliant structural response in the hydrofoil is achieved through local compression flange buckling in the spar.

catamarans, hydrofoils have the potential to enhance the efficiency by lifting the hulls out of the water. Hydrofoils resemble a L-shaped cantilever wing-like structure, which due to its geometry generates a horizontal and a vertical oriented hydrodynamic force, termed side force and lift, respectively. The side-force counteracts the force in the sail and causes the catamaran to accelerate while the lift heaves the hulls above the water surface. At increased speeds hydrofoils generate sufficient lift to keep the catamaran hulls above the water surface, thus reducing drag by reducing wetted surface area. When hydrofoiling, the performance of the catamaran is substantially increased, however, in low speeds, in non-foiling, respectively displacement mode, a drag penalty is created at low speeds from the geometry and surface area necessary for generating the vital lift [20]. This drag penalty could be reduced by passive span-wise bending shape-adaptation which would enable the hydrofoil to have an initially straighter and hence more vertical geometry that could adapt into a L-shaped geometry with increasing speeds. A straight hydrofoil at low speeds generates maximum side-force at minimal induced drag due to the high wing aspect ratio (Fig. 1) [21]. With increasing speed and resulting shape-adaptation, the lift generating wing area increases continuously and generates maximum lift at high speeds (Fig. 1) resulting in optimum configurations in both operation modes.

To fully exploit the concept of a shape-adaptable hydrofoil, buckling in a local area of the compression flange at a pre-determined external bending moment is used to morph the beam. Buckling in the compression flange leads to an in-plane stiffness reduction in the flange and thus enables a beam design with a high pre-buckling and a low post-buckling bending stiffness. The investigated structure is tested using a four-point bending beam which is designed to experience compression flange buckling between the load introductions for a structure and load case of a generic A-Class catamaran hydrofoil [22].

2. Beam models

An analytical four-point bending beam model was developed to enable first approximations of the initial beam bending stiffness, the beam displacement and the bending moment at the point of buckling. Based on the Euler-Bernoulli beam model [23], the stiffness properties were computed using classical laminate theory [24,25]. The four-point bending beam cross-section was modelled with top, bottom, and shear web laminates (Fig. 2, cross-section). The span of the beam was divided into three sections (Fig. 2, side view), each with a separate set of top, bottom, and shear web laminates.

The critical buckling load was calculated by treating the top laminate of Section 2 (Fig. 2 side view) as a long plate with fully constraint unloaded edges parallel to the beam and simply supported loaded edges across the beam. The critical buckling load of such a constrained composite plate is given as [24]:

$$N_{xcr} = \frac{\pi^2}{b^2}\left(D_{11}\frac{b^2}{l_x^2} + 5.139D_{22}\frac{l_x^2}{b^2} + 2.62(D_{12} + 2D_{66})\right). \quad (1)$$

where N_{xcr} is the critical in-plane force per unit width at which the plate buckles, D_{ij} are the bending stiffness matrix components, b is the plate width and l_x is the buckling half-wave length. The buckling halve-wave length is the length that results in the lowest N_{xcr}. The buckling plate dimensions were defined by the length of Section 2 (Fig. 2) and the effective buckling field width.

Eq. (1) is only valid for special orthotropic laminates ($D_{13} = D_{23} = 0$) [24]. Despite a possible overestimation in critical buckling load for fully constrained laminates which are non-special orthotropic ($D_{13} = D_{23} \neq 0$) [27] Eq. (1) was used for a quasi-isotropic laminate in absence of a suitable closed formed expression.

2.1. Finite element model

A finite element model was created in ABAQUS® Standard/FEA and comprised only the non-linear compliant section of the four-point bending beam (Section 2 in Fig. 2) with a constant bending moment. The model was partitioned in the area of the laminate tapers for modelling all ply drop-offs in the beam section (Fig. 3). The ends of the non-linear compliant beam section were connected to reference nodes placed in the cross-section centre of the beam section at the ends of the buckling laminate. The nodes from the cross-section edges were connected to the reference point using kinematic coupling [28], blocking all six degrees of freedom (Fig. 3). The beam section was simply supported at the reference nodes and the long edges of the half beam section were constrained by symmetry constraints (Table 1). The difference in fibre modulus between tension and compression (Table 3) was accounted for by modelling the beam section above the neutral-axis with compressive material properties, and the laminate in the tension side of the beam section below the neutral axis with tensile material properties. The finite element model was meshed with quadratic shell elements (S8R), 0.53×0.53 mm in size for the top laminate and the adjacent radii, and 0.53×1.6 mm in size for the shear webs and the bottom laminate. The resulting accuracy with these element sizes was checked in a mesh convergence study. The composite beam section was analysed using the modified Riks method [29] to predict the post-buckling behaviour.

3. Beam design, material, and manufacturing

The beam section dimensions were selected such that the beam matches the spar of an A-Class catamaran hydrofoil structure with a chord length of 194 mm. The outside beam dimensions (Fig. 4), are 1200 mm in length, 60 mm in width and 15 mm in height with an edge radius of 3.5 mm. The buckling field is 400 mm long, which results in a length to width ratio of approximately 7.55.

The laminate lay-up was selected to comprise fibre angles of 0°, ±45° and 90°, enabling a fibre angle change between each ply of 45°. However, preliminary design iterations showed that 90° plies experienced early matrix tension failure in the bottom laminate and therefore were replaced with ±15° plies. The thickness of the buckling field laminate was 1.6 mm and 3.2 mm for the top laminate in the levers and the complete bottom laminate. The resulting laminate lay-ups used in the finite element model and manufacturing are given in Table 2. The analytical model required an approximation of the shear web because

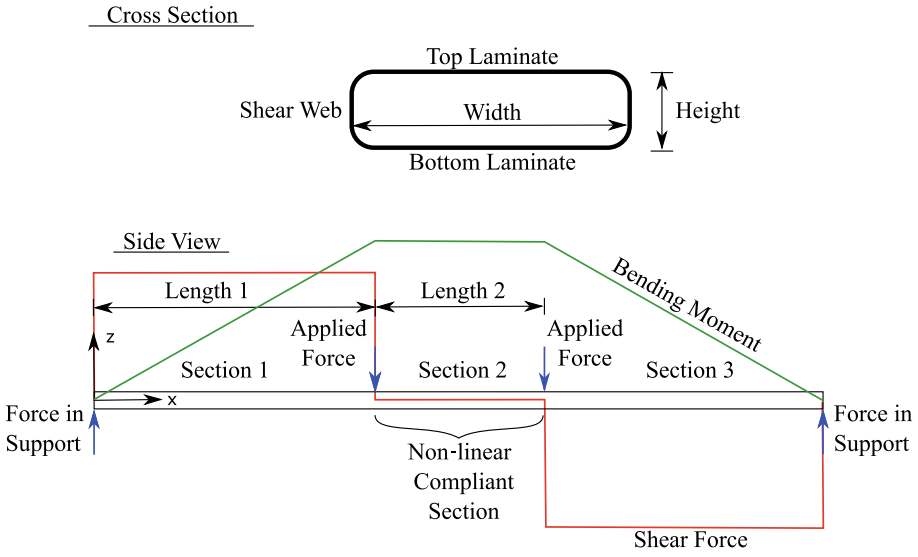

Fig. 2. Top: cross-section of the four-point bending beam; **Bottom**: free body diagram of the four point-bending beam [26].

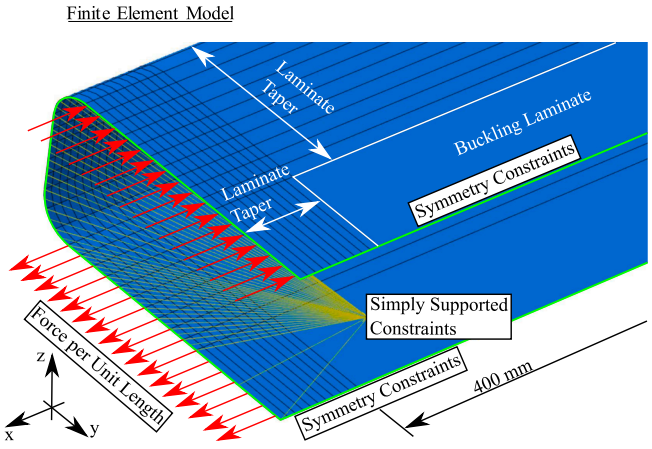

Fig. 3. Finite element model of Section 2 without mesh, showing the transition of Section 1 to Section 2 of the four-point bending beam [26].

Table 1
Table of all degrees of freedom blocked by the constraints.

Constraint	Translation	Rotation
Symmetry	y	x, z
Simply Support End 1	y, z	x, z
Simply Support End 2	x, y, z	x, z

Table 2
Beam laminate layup.

Top laminate	Buckling field laminate	Bottom laminate
[90°	[90°	[−45°
−45°	−45°	45°
90°	90°	−15°
45°	45°	15°
90°	0°	−45°
−45°	−45°	45°
90°	0°	0°
45°	45°]$_S$	−45°
0°		0°
−45°		45°
0°		−15°
45°		15°
0°		0°
−45°		−45°
0°		0°
45°]$_S$		45°]$_S$

only symmetric laminates could be analysed.

Shear web laminate analytical model:
$[-45°/45°/-15°/15°/-45°/45°/0°/45°/-15°/15°/0°/-45°]_S$,
with $E_{11c} = 130$ GPa.

For the bottom, top, and buckling laminate the lay-ups were identical to Table 2. The ply thickness was estimated to be 0.1 mm in the analytical

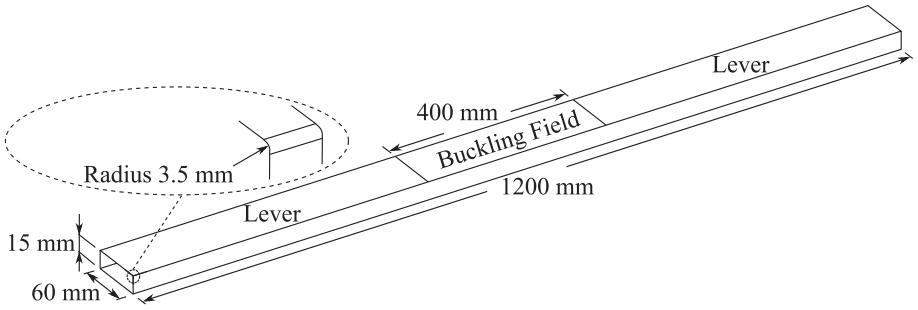

Fig. 4. Four-point bending beam dimensions [26].

Table 3
Prepreg properties for TP135/T800/100 g

Prepreg Properties	Value	Unit
Ply Thickness	0.0953	mm
Fibre Aerial Weight	100	g/m^2
Fibre Volume	60	%
Tensile Modulus E_{11T}	160	GPa
Compression Modulus E_{11C}	130	GPa
Young's Modulus $E_{22,T=C}$	9.0	GPa
Shear Modulus $G_{12} = G_{13}$	4.7	GPa
Shear Modulus G_{23}	4.7	GPa
Poisson's Ratio ν_{12}	0.3	–

model.

The prepreg was manufactured by North Thin Ply Technology with the material properties shown in Table 3.

3.1. Manufacturing

The four-point bending beam was manufactured with a top laminate and a bottom laminate, which were bonded together in a successive manufacturing step. The top laminate was designed as an U-shape to ensure precise manufacturing of the ply drop-offs and buckling field (Fig. 5). The bottom laminate was designed as a C-shape, which provided a good stiffness transition in the area of the buckling field and increased the bond area.

The four-point bending beam was manufactured in three consecutive steps using a heated aluminium mould and an inserted plastic bag for pressure application during curing. The top laminate was draped first and cured at 135 °C and 6 bar pressure, according to specifications of the prepreg manufacture (Fig. 5). In the second step the bottom laminate was draped and cured onto the top laminate with a spacer foil in between (Fig. 5). With this method a constant bondline thickness was ensured. Finally, the top and bottom laminates were prepared using 320 grit sandpaper and bonded using Resoltech 3350/3357T structural adhesive [30](Fig. 6).

4. Experiment

The load-displacement curve was measured with a custom-built four-point bending jig on a Zwick universal testing machine equipped with a 100 kN load cell. The load introductions of the four-point bending jig were set 0.4 m apart, and the beam supports were set 0.375 m away from the load introductions (Fig. 7). The load was introduced through steel loading pins with a 20 mm diameter, fixed to the jig such that the pins could rotate around their axis. The beam supports were 60 mm wide aluminium plates, pivoting around a steel pin. The test displacement speed was set to 10 mm/min. The resulting bending moment M between the load introductions (Eq. (2)) was calculated as the product of the applied force F at one of the load introductions and the resulting distance between the load introduction and beam support (Fig. 7).

$$M = \frac{F}{2}\sqrt{Z_i^2 + 0.375^2} \tag{2}$$

The tensile machine measured the displacement between the load introductions and the beam supports Z. In the finite element analysis, only the non-linear compliant section was simulated, therefore, only the beam mid-span displacement ζ of the non-linear compliant beam section relative to the load introductions was known. For comparing the experimental results with the simulation, the displacement results Z_i were converted by measuring Z and ζ at the maximum displacement in the experiment and scaling the displacement results Z_i accordingly to ζ_i (Eq. (3)).

$$\zeta_i = Z_i \cdot \zeta_{\mathbf{max}} / Z_{\mathbf{max}} \tag{3}$$

The buckling field deformation was scanned with a stereoscopic camera during the four-point bending test. The stereoscopic camera was a GOM ATOS III Rev. 02 with a measuring volume of 320 × 240 × 240 mm and a scanning frequency of 1 Hz. The buckling field was primed with white paint onto which black speckles were sprayed in a random pattern. The pattern was detected with a precision of ± 0.02 mm. The scans were analysed with the software Aramis Professional 2016. The digital image correlation (DIC) data was read out across the buckling field along two parallel lines. These were placed along the longitudinal centre line and the beam edge. The scan procedure started by placing the beam into the four-point bending jig without applying a load. At this position, a static reference scan was made to which all following measurements were related to. After the reference was established the four-point bending test and scanning was started.

For data processing the load-displacement curve of the finite element model and the experiment were approximated by cubic splines. For determining the bending angle at the load introductions the beam bending deformation measured with DIC at the beam edge was idealized with the circle equation assuming a constant bending moment and a constant inertia between the load-introductions. The equation was fitted by minimizing the sum of least squares of the radial deviation.

5. Results and discussion

The load-displacement curve of the experiment, the finite element model and the analytical model show very good agreement up to the point of buckling (Fig. 8).

As would be expected, the analytical model only captures the load-displacement behaviour until the onset of buckling. In post-buckling, after an initial 10% buckling load increase, the load-displacement curve of the finite element model starts to deviated from the experimental measurement (Fig. 8 and 9). The experimental data in post-buckling demonstrates a saw-tooth patterned noise as a result of the beam sliding on the supports in a stick-slip fashion while undergoing large deformation. The load-displacement results exhibit a kink, indicating that following the point of buckling, a desired reduction in bending stiffness can be achieved.

The bending moment at the point of buckling M_{buckling} was determined by the point of inflection ($M''(\zeta) = 0$) in the bending stiffness-displacement plot (Fig. 9). For the experiment, $M_{\text{E buckling}}$ is at 374.8 Nm, while $M_{\text{F buckling}}$ is at 374.20 Nm predicted by the finite element model, which results in a difference of 0.16% relative to the experiment. In comparison, the analytically derived $M_{\text{A buckling}}$ is at 386.50 Nm, which results in an error of 3.1%, relative to the experiment. The analytically and numerically determined M_{buckling} agree very well with the experiment in spite of several simplifications. These very good agreements of

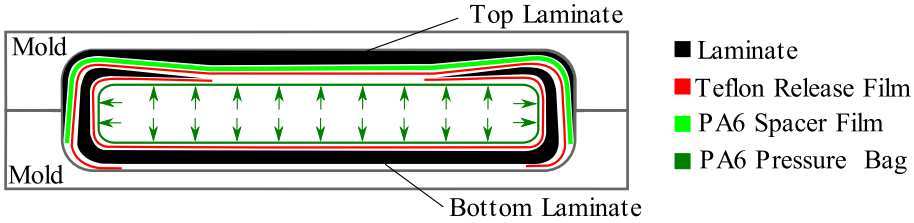

Fig. 5. Manufacturing of top and bottom laminate.

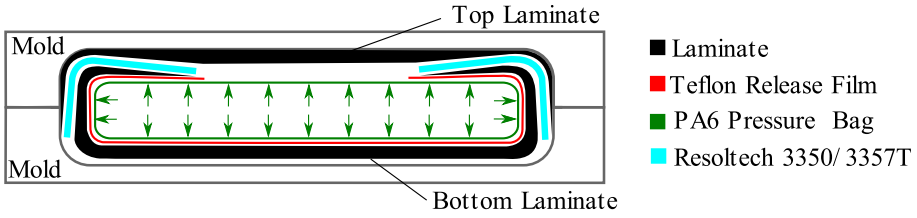

Fig. 6. Joining of top and bottom laminate.

$M_{buckling}$ give confidence that compression flange buckling can be precisely tailored to a desired buckling load.

The bending stiffness, which is the first derivative of the load-displacement curve is shown in Fig. 9. The initial bending stiffness showed a very good agreement between the analytical model, the finite element model and the experiment, with a maximal difference of 3.8% relative to the experiment. Leading up to the point of buckling the bending stiffness was predicted to reduce by 28% in the finite element model and measured to be 29% in the experiment. At 10% $M_{buckling}$ increase the initial bending stiffness is reduced by 41% in the finite element model and by 42% in the experiment. As a result of the increased compliance a bending angle α of 9.15° (as defined in Fig. 7) was achieved in the experiment at the point of ultimate failure. A stiffness reduction in excess of 42% and a bending angle of 9.15° shows the effectiveness of compression flange buckling to achieve a non-linear bending compliance, which provides the validity of the structural concept.

In the experiment, ultimate failure occurred suddenly, without warning at 524 Nm. The location of failure in the top laminate is at the beam mid-span where the buckling field laminate failed in compression (Fig. 10). Secondary failure occurred in the bottom laminate in compression likely due to excessive bending after the buckling laminate had failed. The occurring delaminations were very local, with the largest delamination reaching a length of approximately 30 mm, which indicates that the beam can be designed to safety limits that are close to the beams ultimate strength without risk of damage accumulation during service operation. The finite element model predicted first ply failure in matrix tension at 468 Nm and an on-set of fibre compression failure at 480 Nm with Hashin's failure criteria. With a difference of 44 Nm between the predicted on-set of fibre compression failure and measured ultimate failure, the results show a good correlation between the finite element model and the experiment.

The DIC results allow a closer analysis of the buckling field deformation and the resulting surface strains. The agreement of DIC results with finite element results was evaluated at two points of load-displacement, the point of buckling and the point of compressive fibre failure, as defined in Fig. 8.

In Fig. 11 the out-of-plane displacements are shown for the finite

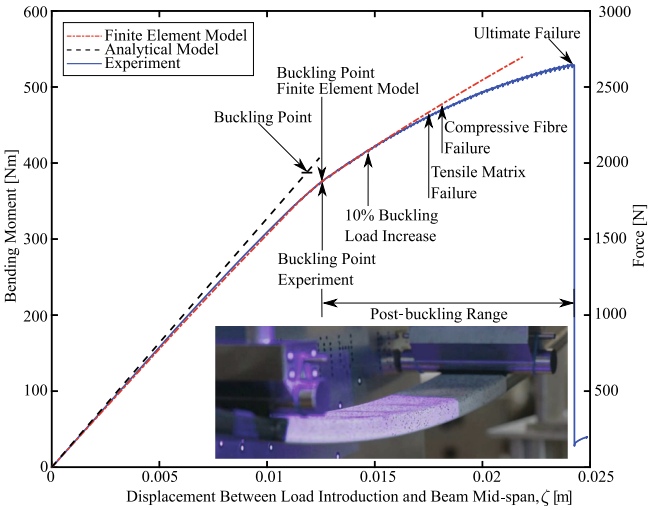

Fig. 8. Analytical, numerical, and experimental load-displacement curves. Photograph in the lower right corner shows the bucking field at 10% buckling load increase [26].

element model and the experiment. For clarity, the mean beam section displacement was subtracted from the out-of-plane displacement.

The predicted buckling mode shape of the finite element model was verified as 15 sine shaped half-waves and a single transverse wave, which was visually confirmed in the experiment. This was also confirmed by the good agreement in average buckling half-wave length, which was predicted as 28.2 ± 0.2 mm in the finite element model and measured as 27.0 ± 0.3 mm in the experiment at the point of fibre compression failure.

The amplitudes of the buckling half-waves are not constant in value across the buckling field at the point of buckling. In the finite element model the amplitudes decrease towards the beam mid-span. This was not the case for the experiment which shows large irregular changes in amplitude, likely caused by laminate imperfections. At the point of fibre compression failure the amplitude distribution has diminished in the

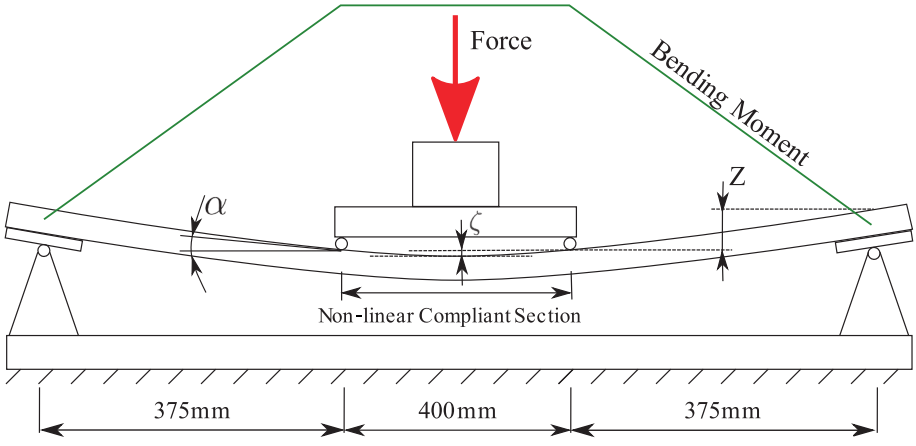

Fig. 7. Dimensions and bending moment distribution of the four-point bending test [26].

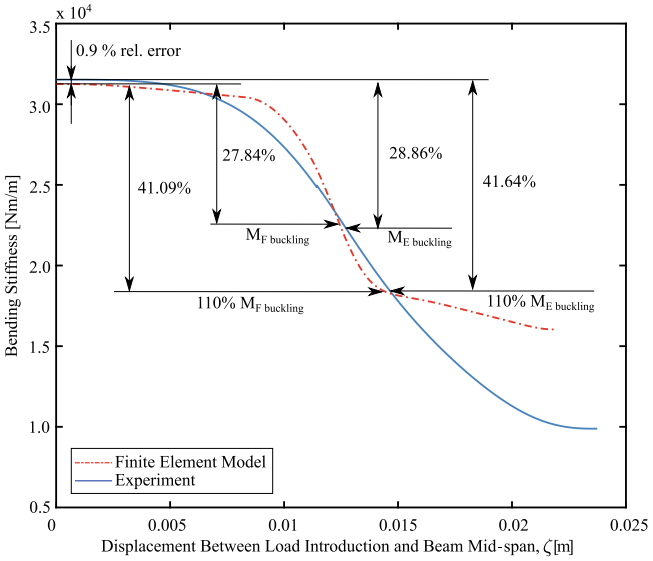

Fig. 9. Change in beam bending stiffness with increasing beam displacement for the finite element model and the experiment [26].

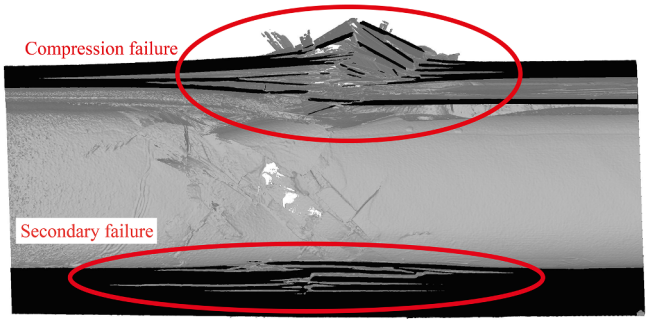

Fig. 10. Computer tomographic scan of failed buckling section. Cut along longitudinal center plane.

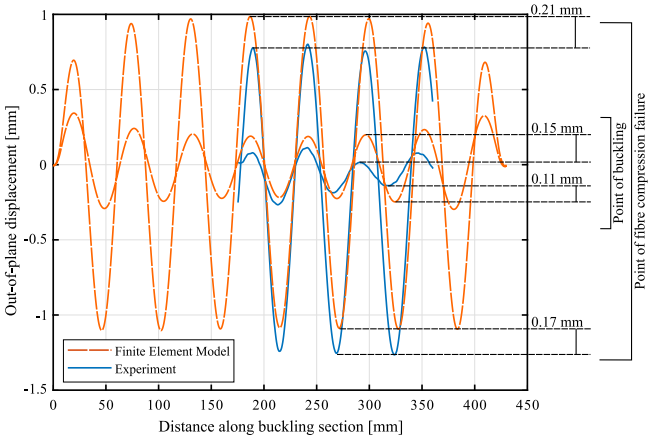

Fig. 11. Out-of-plane displacement of buckling field.

finite element model and the experiment. The average peak-to-peak amplitude in the buckling field is 2.06 ± 0.2 mm and 2.03 ± 0.2 mm, as predicted by the finite element model and measured by the experiment, respectively.

Interestingly, the amplitude average has moved towards the beam cross-section centre in the finite element model and the experiment. This was attributed to anticlastic laminate deformations which are a reaction to the strong beam bending. At the point of fibre compression failure, the off-set was predicted as −0.06 mm in the finite element

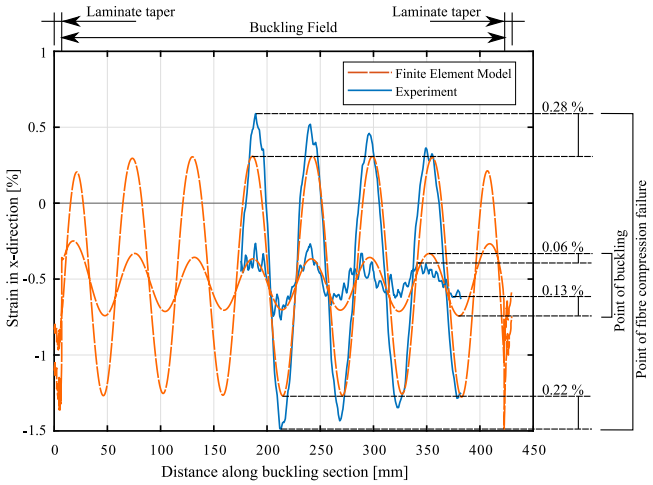

Fig. 12. Surface strain distribution across the buckling field at the point of buckling and the point of fiber compression failure.

model and measured as −0.24 mm in the experiment.

The out-of-plane displacements create varying surface strains along the beam axis, shown in Fig. 12. The strain curves of the experiment show some noise, especially at the point of buckling which is an artefact of the DIC resolution. In general the surface strain pattern follows the out-of-plane displacement pattern of Fig. 11, with a compressive strain at a buckling wave trough and a tensile strain at a buckling wave peak. The only exception in these results are the surface strain amplitudes which increase towards the beam mid-span at the point of fibre compression failure, unlike the corresponding out-of-plane displacements amplitudes. This result is an indication for imperfections in the laminate thickness resulting in non-uniform strain distributions.

The maximum surface strain amplitudes are located at the buckling wave troughs, with a compressive surface strain of −1.26 ± 0.01% for the finite element model and −1.39 ± 0.08% for the experiment at the point of fibre compression failure. The corresponding maximum tensile surface strain is 0.3 ± 0.01% for the finite element model and 0.48 ± 0.08% for the experiment.

The reason for the surface tensile strain magnitude being smaller than for the surface compressive strain is the off-set in strain amplitude average. In the finite element model, the strain amplitude average is predicted at −0.53% at the point of buckling and −0.48% at the point of fibre compression failure. The experimental measurements indicated −0.49% at the point of buckling and at −0.45% at the point of fibre compression failure. The dominating load in the buckling laminate seems, therefore to be a compressive load and does not change much while the peak-to-peak amplitude strongly increases.

The good agreement between DIC results and the finite element model show that the local deformations of a buckling field were captured accurately by the finite element model. This shows that it is therefore possible to design and optimize the buckling field locally and encourages further use of post-buckling in non-linear compliant structures.

With the knowledge gained in this work, we applied the principle of local compression flange buckling to a realistic case in the root section of a hydrofoil of a sailing catamaran. In order to assess the performance increase a velocity prediction program (VPP) has been used. It solves the equation of motion by balancing the forces and moments from the sail, the hull and the hydrofoils. The drag and lift polars have been solved by vortex lattice panel method taking into account the different deformed states of the hydrofoil. In each sailing condition the VPP minimizes drag by finding best trim settings of sail, crew weight, rudder angle and hydrofoil rake angle, etc. within set bounds.

Due to the lateral forces on the vessel, the leeward foil deforms as schematically illustrated in Fig. 1, while the windward foil maintains its

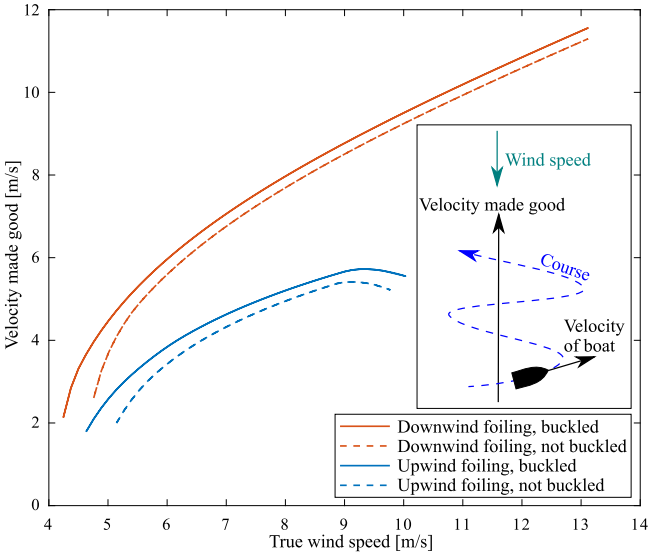

Fig. 13. Preliminary velocity made good predictions (meaning velocity to windward/downwind) of an A-class catamaran in hydrofoiling sailing conditions, comparing a hydrofoil with nonlinear (buckled) compliance with a conventional configuration. The benefit of a compliance adds about 3% speed, whereas the benefits as well as the differences of onsets of foiling are more substantial in low speed conditions.

shape, resulting in an asymmetric configuration.

The results shown in Fig. 13 are very promising, showing an average increase in velocity made good of 3% compared to the best fully optimized conventional configurations. A hydrofoil that transitions from a conventional configuration to a buckled configuration at low true wind speeds will therefore increase the performance of the boat noticeably. This application study highlighted the applicability of local compression flange buckling to practical applications for drag reduction and thus energy saving.

6. Conclusions

In this work, a span-wise non-linear bending compliance was, for the first time, reported in carbon-fibre reinforced polymer beams at high loads using local buckling in the compression flange. This structural concept is suitable for passive span-wise bending shape-adaptation in wing-like structures and would enable a change in shape from a straight geometry into a strongly bent geometry without the need for actuators. Such change in geometry may increase efficiency and manoeuvrability of highly loaded wings. The concept was developed analytically and numerically on a four-point bending beam and validated in an experiment. The results show a very high agreement with errors below 5% relative to the experiment. A bending stiffness reduction of 41.64% due to local flange buckling and a post-buckling loading range of 40% the buckling load shows the effectiveness of the structural concept for non-linear bending compliance, and will enable the realisation of highly loaded structures with programmable post-buckling behaviour. This design technique in combination with new materials [3,4,6], that combine enhanced design freedom and high mechanical performance could prove a breakthrough in several lightweight structural applications.

Declaration of Competing Interest

The authors declare that they have no known competing financial interests or personal relationships that could have appeared to influence the work reported in this paper.

Acknowledgement

This research was part of the project “Efficient hydrofoils with nonlinear compliance (EHYComp)” No.19038.1 PFIW-IW and supported by the Swiss Innovation Agency, Innosuisse. Further, we would like to acknowledge the support of lead engineer Stephane Dyen from ENATA Industries FZE with the velocity prediction program (VPP) and Oliver Focke from the Faserinstitut Bremen for the computer tomographic scan.

Appendix A. Supplementary data

Digital image correlation videos showing the displacement and strain development in the buckling field are provided online. Supplementary data associated with this article can be found, in the online version, at https://doi.org/10.1016/j.compstruct.2020.111995.

References

[1] Campanile L. Being lightweight: a crucial requirement. Wagg D, Bond I, Weaver P, Friswell M, editors. Adaptive Structures Engineering Applications, Ch. 4.4. Chichester, UK: John Wiley & Sons Ltd; 2007. p. 95–104.
[2] Barbarino S, Bilgen O, Ajaj RM, Friswell MI, Inman DJ. A review of morphing aircraft. J Intell Mater Syst Struct 2011;22(9):823–77.
[3] Amacher R, Cugnoni J, Botsis J, Sorensen L, Smith W, Dransfeld C. Thin ply composites: experimental characterization and modeling of size-effects. Compos Sci Technol 2014;101:121–32.
[4] Cugnoni J, Amacher R, Kohler S, Brunner J, Kramer E, Dransfeld C, Smith W, Scobbie K, Sorensen L, Botsis J. Towards aerospace grade thin-ply composites: Effect of ply thickness, fibre, matrix and interlayer toughening on strength and damage tolerance. Compos Sci Technol 2018;168(September):467–77.
[5] Teixeira RF, Pinho ST, Robinson P. Thickness-dependence of the translaminar fracture toughness: experimental study using thin-ply composites. Compos Part A: Appl Sci Manuf 2016;90:33–44.
[6] Gantenbein S, Masania K, Woigk W, Sesseg JP, Tervoort TA, Studart AR. Three-dimensional printing of hierarchical liquid-crystal-polymer structures. Nature 2018;561(7722):226–30.
[7] Filipovic D, Kress G. Manufacturing method for high-amplitude corrugated thin-walled laminates. Compos Struct 2019;222:110925.
[8] Tridech C, Maples HA, Robinson P, Bismarck A. High performance composites with active stiffness control. ACS Appl Mater Interfaces 2013;5(18):9111–9.
[9] Hayat K, Ha SK. Load mitigation of wind turbine blade by aeroelastic tailoring via unbalanced laminates composites. Compos Struct 2015;128:122–33.
[10] Motley MR, Liu Z, Young YL. Utilizing fluid-structure interactions to improve energy efficiency of composite marine propellers in spatially varying wake. Compos Struct 2009;90(3):304–13.
[11] Arrieta AF, Kuder IK, Rist M, Waeber T, Ermanni P. Passive load alleviation aerofoil concept with variable stiffness multi-stable composites. Compos Struct 2014;116:235–42.
[12] Runkel F, Reber A, Molinari G, Arrieta AF, Ermanni P. Passive twisting of composite beam structures by elastic instabilities. Compos Struct 2016;147:274–85.
[13] Cordisco P, Bisagni C. Cyclic buckling tests of stiffened composite curved panels under compression and shear. In: 49th AIAA/ASME/ASCE/AHS/ASC Structures, Structural Dynamics, and Materials Conference 16t, Schaumburg, IL, USA (2008) 1–19.
[14] Wiggins LD, Stubbs MD, Johnston CO, Robertshaw HH, Reinholtz CF, Inman DJ. A design and analysis of a morphing Hyper-Elliptic Cambered Span (HECS) wing. In: 45th AIAA/ASME/ASCE/AHS/ASC Structures, Structural Dynamics & Materials Conference, Palm Springs, California, USA; 2004. pp. 1–10.
[15] Ursache NM, Melin T, Isikveren AT, Friswell MI. Technology integration for active poly-morphing winglets development. In: Proceedings of the ASME Conference on Smart Materials, Adaptive Structures and Intelligent Systems, SMASIS2008, vol. 1, Ellicott City, Maryland, USA; 2008. p. 1–8.
[16] Manzo J, Garcia E. Demonstration of an in situ morphing hyperelliptical cambered span wing mechanism. Smart Mater Struct 2010;19(2):1–11.
[17] Sofl A, Meguid S, Tan K, Yeo W. Shape morphing of aircraft wing: Status and challenges. Mater Des 2010;31(3):1284–92.
[18] Moosavian A, Xi F, Hashemi SM. Design and motion control of fully variable morphing wings. J Aircraft 2013;50(4):1189–201.
[19] Lachenal X, Daynes S, Weaver P. Review of morphing concepts and materials for wind turbine blade applications. Wind Energy 2013;16(2):283–307.
[20] Paulin A, Hansen H, Hochkirch K, Fischer M. Performance assessment and optimization of a C-class catamaran hydrofoil configuration. In: 5th High Performance Yacht Design Conference, Auckland; 2015. p. 190–199.
[21] Katz J, Plotkin A. Three-Dimensional Small-Disturbance Solutions. Low-Speed Aerodynamics. 2nd ed.New York: Cambridge University Press; 2001. Ch. 8.
[22] Technical Committee IACA. ISAF International A Class Catamaran-Measurers' Guide, [Date accessed 24.04.2016]; 2016, 1–9.http://www.a-cat.org/?q=node/9.
[23] Gere JM. Mechanics of Materials. 6th ed. Belmont, CA, US: Brooks/Cole-Thomson Learning; 2003.

[24] Kollar LP, Springer GS. Mechanics of composite structures. Cambridge: Cambridge University Press; 2003.
[25] Swanson SR. Analysis of laminated beams. Introduction to Design and Analysis with Advanced Composite Materials. Prentice Hall Engineering/Science/Mathematics; 1997. p. 191–223. Ch. 7.
[26] Schadt F, Rueppel M, Brauner C, Masania K, Dransfeld C, Ricard T. Nonlinear bending compliance of closed-sectioned composite beam structures by local compression flange buckling. ECCM18 – 18th European Conference on Composite Materials Athens 24–28th June Greece. 2018. p. 1–8.
[27] Jones RM. Mechanics of composite materials. 2nd ed. Philadelphia: Taylor & Francis Inc; 1999.
[28] Dassault Systèmes Simulia Corp., Kinematic coupling constraints kinematic. In: Abaqus 6.13 Analysis User's Guide Volume V: Prescribed Conditions, Constraints & Interactions, Providence, RI, USA; 2013. Ch. 35.2.3, p. 1–3.
[29] Dassault Systèmes Simulia Corp., Modefied Riks Algorithm. In: Abaqus 6.13 Theory Guide, Providence, RI, USA; 2013, Ch. 2.3.2, p. 1–5.
[30] Geissberger R, Maldonado J, Bahamonde N, Keller A, Dransfeld C, Masania K, et al. Rheological modelling of thermoset composite processing. Compos Part B: Eng 2017;124:182–9.